

Monthly Weather Review

Comparison of Terrain Following and Cut Cell Grids using a Non-Hydrostatic Model --Manuscript Draft--

Manuscript Number:	MWR-D-15-0226
Full Title:	Comparison of Terrain Following and Cut Cell Grids using a Non-Hydrostatic Model
Article Type:	Article
Corresponding Author:	James Shaw University of Reading Reading, Berkshire UNITED KINGDOM
Corresponding Author's Institution:	University of Reading
First Author:	James Shaw
Order of Authors:	James Shaw Hilary Weller
Abstract:	<p>Terrain following coordinates are widely used in operational models but the cut cell method has been proposed as an alternative that can more accurately represent atmospheric dynamics over steep orography. Because the type of grid is usually chosen during model implementation, it is typically necessary to use different models in order to compare the accuracy of different grids. In contrast, here a single C-grid finite volume model is used to enable a like-for-like comparison of terrain following and cut cell grids.</p> <p>A series of standard two-dimensional tests using idealised terrain are performed: tracer advection in a prescribed horizontal velocity field, a test starting from stably stratified initial conditions, and orographically induced gravity waves described by nonhydrostatic dynamics. In addition, a new tracer advection test is formulated having a velocity field that is everywhere tangential to the terrain following coordinate surfaces. This new test presents a challenge to cut cells in situations with a large Froude number and large Scorer parameter.</p> <p>The results of the advection tests demonstrate that tracer accuracy depends upon alignment of the flow with the grid. As expected, the cut cell grid maintains greater accuracy in the test of stationary, stratified flow. In the gravity waves test, results on all grids are in good agreement with existing results from the literature. However, it is found that the Lorenz computational mode is excited as a vertical zig-zag in potential temperature on the cut cell grid.</p>
Suggested Reviewers:	<p>Daniel Leuenberger Senior Researcher, MeteoSwiss Daniel.Leuenberger@meteoswiss.ch Worked with Christoph Schaer on tracer advection and Schaer waves tests which are used in this paper.</p> <p>Günther Zängl Deutscher Wetterdienst, DWD guenther.zaengl@dwd.de Experience with horizontal pressure gradient errors and mountain flow and resting atmosphere tests</p> <p>Joe Klemp Senior Scientist, National Center for Atmospheric Research klemp@ucar.edu Familiarity with vertical coordinate systems, author of resting atmosphere test</p>

Copyright Form

[Click here to download Copyright Form: copyright.pdf](#)

Comparison of Terrain Following and Cut Cell Grids using a Non-Hydrostatic Model

James Shaw* and Hilary Weller

Department of Meteorology, University of Reading, Reading, United Kingdom

* *Corresponding author address:* Department of Meteorology, University of Reading, Earley Gate,

PO Box 243, Reading, RG6 6BB, UK.

E-mail: js102@zepler.net

ABSTRACT

8 Terrain following coordinates are widely used in operational models but the
9 cut cell method has been proposed as an alternative that can more accurately
10 represent atmospheric dynamics over steep orography. Because the type of
11 grid is usually chosen during model implementation, it is typically necessary
12 to use different models in order to compare the accuracy of different grids. In
13 contrast, here a single C-grid finite volume model is used to enable a like-for-
14 like comparison of terrain following and cut cell grids. A series of standard
15 two-dimensional tests using idealised terrain are performed: tracer advection
16 in a prescribed horizontal velocity field, a test starting from stably stratified
17 initial conditions, and orographically induced gravity waves described by non-
18 hydrostatic dynamics. In addition, a new tracer advection test is formulated
19 having a velocity field that is everywhere tangential to the terrain following
20 coordinate surfaces. This new test presents a challenge to cut cells in situa-
21 tions with a large Froude number and large Scorer parameter. The results of
22 the advection tests demonstrate that tracer accuracy depends upon alignment
23 of the flow with the grid. As expected, the cut cell grid maintains greater
24 accuracy in the test of stationary, stratified flow. In the gravity waves test,
25 results on all grids are in good agreement with existing results from the liter-
26 ature. However, it is found that the Lorenz computational mode is excited as
27 a vertical zig-zag in potential temperature on the cut cell grid.

28 **1. Introduction**

29 Representing orography accurately in numerical weather prediction systems is necessary to
30 model downslope winds and local precipitation. Orography also exerts strong non-local influ-
31 ences: from the latent heat release due to convection, by directly forcing planetary waves, and by
32 the atmospheric response to form drag and gravity wave drag. There are two main approaches to
33 represent orography on a grid: terrain following layers and cut cells. Both methods align cells in
34 vertical columns. Because most models are designed for a particular type of grid, existing stud-
35 ies of cut cell solutions have compared results with terrain following grid solutions implemented
36 within different models, for example Good et al. (2014). Instead, this study uses a single model to
37 enable a like-for-like comparison between solutions using terrain following and cut cell grids.

38 With increasing horizontal model resolution, the discrete representation of terrain can become
39 steeper, making accurate calculation of the horizontal pressure gradient more difficult when using
40 terrain following layers (Gary 1973; Steppeler et al. 2002). Numerical errors in this calculation
41 result in spurious winds and can cause numerical instability (Fast 2003; Webster et al. 2003). Cut
42 cell methods seek to reduce the error that is associated with steep orography.

43 With terrain following (TF) layers the terrain’s influence decays with height so that the bot-
44 tommost layers follow the underlying surface closely while the uppermost layers are flat. There
45 are two main approaches to minimizing errors associated with TF layers. First, by smoothing
46 the effects of terrain with height, the influence of the terrain is reduced, hence errors in the cal-
47 culated horizontal pressure gradient are also reduced aloft (Schär et al. 2002; Leuenberger et al.
48 2010; Klemp 2011). However, the error is not reduced at the ground where steep terrain remains
49 unmodified.

50 Second, numerical errors can also be reduced by improving the accuracy in calculating the hor-
51 izontal pressure gradient itself. TF layers are usually implemented using a coordinate transforma-
52 tion onto a rectangular computational domain, which introduces metric terms into the equations of
53 motion. The techniques proposed by Klemp (2011) and Zängl (2012) both involve the calculation
54 of the horizontal pressure gradient in the physical domain. This gave them the flexibility to design
55 more accurate horizontal pressure gradient discretizations using more appropriate stencils.

56 Despite their associated numerical errors, TF layers are in widespread operational use (Steppeler
57 et al. 2003). They are attractive because their rectangular structure is simple to process by com-
58 puter and link with parameterisations, boundary layer resolution can be increased with variable
59 spacing of vertical layers (Schär et al. 2002), and cell sizes remain almost constant (Jebens et al.
60 2011).

61 Cut cells is an alternative method in which the grid does not follow the terrain but, instead, cells
62 that lie entirely below the terrain are removed, and those that intersect the surface are modified in
63 shape so that they more closely fit the terrain. The resulting grid is orthogonal everywhere except
64 near cells that have been cut. Hence, errors are still introduced when calculating the horizontal
65 pressure gradient between cut and uncut cells.

66 The cut cell method can create some very small cells which reduce computational efficiency
67 (Klein et al. 2009), and several approaches have been tried to alleviate the problem (Steppeler
68 et al. 2002; Yamazaki and Satomura 2010; Jebens et al. 2011).

69 Several studies have shown examples where cut cells produce more accurate results when com-
70 pared to TF coordinates. Spurious winds seen in TF coordinates are not present with cut cells and
71 errors do not increase with steeper terrain (Good et al. 2014). A comparison of TF and cut cells
72 using real initial data by Steppeler et al. (2013) found that five-day forecasts of precipitation and
73 wind over Asia in January 1989 were more accurate in the cut cell model.

74 Another alternative method is the eta coordinate, described by Mesinger et al. (1988). This
75 transformation, expressed in pressure coordinates, quantises the surface pressure at each grid box
76 using prescribed geometric heights. This results in terrain profiles having a staircase pattern which
77 is known as ‘step’ orography. The eta coordinate improves the accuracy of the horizontal pressure
78 gradient calculation compared to the sigma coordinate (Mesinger et al. 1988).

79 In an experiment of orographically induced gravity waves, Gallus and Klemp (2000) found that
80 horizontal flow along the lee slope was artificially weak. Mesinger et al. (2012) offer an expla-
81 nation for this behaviour: air flowing along the lee slope cannot travel diagonally downwards but
82 must first travel horizontally, then vertically downward. However, lee slope winds are weakened
83 because some of the air continues to be transported horizontally aloft.

84 Mesinger et al. (2012) refined the formulation to allow diagonal transport of momentum and
85 temperature immediately above sloping terrain. This arrangement is similar to the finite volume
86 cut cell method. The new method improved test results, increasing lee slope winds by 4 m s^{-1} to
87 5 m s^{-1} (Mesinger et al. 2012).

88 This study uses a modification of the fully-compressible model from Weller and Shahrokhi
89 (2014) to enable a like-for-like comparison between terrain following and cut cell grids for ide-
90 alised, two-dimensional test cases from the literature. Section 2 presents the formulation of the
91 terrain following and cut cell grids used in the experiments that follow. In section 3 we give the
92 governing equations, outline the model from Weller and Shahrokhi (2014) and describe the modi-
93 fication which improves stability for long timesteps in the presence of steep orography. Section 4
94 analyses the results from two tracer advection tests, a test of a stably stratified atmosphere initially
95 at rest, and orographically induced gravity waves. Concluding remarks are made in section 5.

96 2. Grids

97 Here we describe the formulation of the terrain following grids and the method of cut cell grid
98 construction. The techniques presented are used to define the grids for the experiments in the
99 subsequent section.

100 Gal-Chen and Somerville (1975) proposed a basic terrain following (BTF) coordinate defined
101 as

$$z = (H - h)(z^*/H) + h \quad (1)$$

102 where, in two dimensions, $z(x, z^*)$ is the physical height of the coordinate surface at level z^* , H is
103 the height of the domain, and $h(x)$ is the height of the terrain surface. In this formulation z^*/H
104 ranges from 0 to 1. Using this coordinate, the terrain's influence decays linearly with height but
105 disappears only at the top of the domain. An example is shown in figure 1a.

106 The sigma coordinate transform of Phillips (1957) is equivalent to the BTF coordinate transform
107 since they both decay linearly. However, because $\sigma = p/p_s$ decays with pressure rather than
108 height, sigma coordinates also vary with surface pressure, $p_s(x, t)$.

109 The hybrid terrain following (HTF) coordinates of Simmons and Burridge (1981) improve upon
110 BTF coordinates by using a decay function that allows the influence of the terrain to be removed
111 at a specified height, producing model layers aloft that have constant pressure.

112 The smooth level vertical (SLEVE) coordinate proposed by Schär et al. (2002) achieves a more
113 regular TF grid in the middle and top of the domain than the BTF coordinate. The terrain height
114 is split into large-scale and small-scale components, h_1 and h_2 , such that $h = h_1 + h_2$, with each
115 component having a different exponential decay. The transformation is defined as

$$z = z^* + h_1 b_1 + h_2 b_2 \quad (2)$$

116 where the vertical decay functions are given by

$$b_i = \frac{\sinh((H/s_i)^n - (z^*/s_i)^n)}{\sinh(H/s_i)^n} \quad (3)$$

117 with s_1 and s_2 are the scale heights of large-scale and small-scale terrain respectively. The exponent
118 n was introduced by Leuenberger et al. (2010) in order to increase cell thickness in the layers
119 nearest the ground, allowing longer timesteps. Leuenberger et al. (2010) found the exponent has
120 an optimal value of $n = 1.35$. Choosing $n = 1$ gives the decay functions used by Schär et al.
121 (2002). An example of the SLEVE grid can be seen in figure 1b.

122 Most implementations of terrain following layers use a coordinate system that makes the domain
123 rectangular, but introduces metric terms into the equations of motion. Instead, the model employed
124 in this study uses Cartesian coordinates and unstructured grids. By doing so, results from the
125 same model can be compared between terrain following and cut cell grids without modifying the
126 equation set or discretisation.

127 The OpenFOAM utility `snappyHexMesh` was used to create a grid that approximates the cut
128 cell method. First, a custom utility was used to move points beneath the surface up to the surface
129 creating small cells near mountain peaks. Second, the surface faces were taken from the BTF
130 grid and `snappyHexMesh` was used to intersect the surface with the grid. This tool removes cells
131 whose centres are below the surface and displaces boundary vertices so that they are ‘snapped’ to
132 the BTF surface (OpenCFD Foundation cited 2015). An example of the resulting grid is shown in
133 figure 1c.

134 There are two details of grid construction which mean that resulting cut cell grids can differ
135 slightly from a typical cut cell grid created using a shaving method, as described by Adcroft et al.
136 (1997). First, when `snappyHexMesh` moves vertices onto the terrain surface, some points are
137 moved horizontally. Second, the utility does not create new points necessary for pentagonal cells.

3. Model

We use the finite volume model from Weller and Shahrokhi (2014) which details a C-grid discretisation of the fully-compressible Euler equations, given by

$$\text{Momentum} \quad \frac{\partial \rho \mathbf{u}}{\partial t} + \nabla \cdot \rho \mathbf{u} \mathbf{u} = \rho \mathbf{g} - c_p \rho \theta \nabla \Pi \quad (4a)$$

$$\text{Continuity} \quad \frac{\partial \rho}{\partial t} + \nabla \cdot \rho \mathbf{u} = 0 \quad (4b)$$

$$\text{Thermodynamic equation} \quad \frac{\partial \rho \theta}{\partial t} + \nabla \cdot \rho \mathbf{u} \theta = 0 \quad (4c)$$

$$\text{Ideal gas law} \quad \Pi^{(1-\kappa)/\kappa} = \frac{R \rho \theta}{p_0} \quad (4d)$$

where ρ is the density, \mathbf{u} is the velocity field, \mathbf{g} is the gravitational acceleration, c_p is the heat capacity at constant pressure, $\theta = T(p_0/p)^\kappa$ is the potential temperature, T is the temperature, p is the pressure, p_0 is a reference pressure, $\Pi = (p/p_0)^\kappa$ is the Exner function of pressure, and $\kappa = R/c_p$ is the gas constant to heat capacity ratio.

The model uses a Lorenz C-grid staggering of thermodynamic variables such that θ , ρ and Π are stored at cell centres and the covariant component of velocity at cell faces.

A minor change has been made to the curl-free, non-orthogonal formulation as described in Weller and Shahrokhi (2014) to improve stability on non-orthogonal grids. Weller and Shahrokhi (2014) use a Hodge dual operator, H , to map from co-variant to contra-variant velocity components:

$$U = HV \quad (5)$$

where $U = \rho \mathbf{u} \cdot \mathbf{S}_f$ and $V = \rho \mathbf{u} \cdot \mathbf{d}_f$. \mathbf{S}_f is the surface normal vector for a face, f , which has a magnitude of the surface area, and \mathbf{d}_f is the vector between neighbouring cell centres.

In order to create a semi-implicit formulation, Weller and Shahrokhi (2014) split H into diagonal and off-diagonal components and the off-diagonal components are treated explicitly in the

155 Helmholtz equation for Π . However, this was found to be unstable when using a large timestep
 156 on a grid with large non-orthogonality. Improved stability is achieved by splitting H into the
 157 orthogonal part and the non-orthogonal correction:

$$H = H_c + H_{\text{corr}} \quad (6)$$

158 where the diagonal matrix $H_c = |\mathbf{S}_f|/|\mathbf{d}_f|$ and the non-orthogonal correction is simply $H_{\text{corr}} =$
 159 $H - H_c$. The orthogonal part, H_c , is treated implicitly in the Helmholtz equation and the non-
 160 orthogonal part, H_{corr} , is treated explicitly.

161 For tracer advection tests, the advection equation in flux form, given by

$$\partial\phi/\partial t + \nabla \cdot (\mathbf{u}\phi) = 0 \quad (7)$$

162 is solved using the upwind-biased multidimensional cubic scheme from Weller and Shahrokhi
 163 (2014) which is non-monotonic and not flux corrected. The time derivative is solved using a
 164 three-stage, second order Runge-Kutta scheme:

$$\phi^* = \phi^{(n)} + \Delta t f(\phi^{(n)}) \quad (8a)$$

$$\phi^{**} = \phi^{(n)} + \frac{\Delta t}{2} \left(f(\phi^{(n)}) + f(\phi^*) \right) \quad (8b)$$

$$\phi^{(n+1)} = \phi^{(n)} + \frac{\Delta t}{2} \left(f(\phi^{(n)}) + f(\phi^{**}) \right) \quad (8c)$$

165 where $f(\phi^{(n)}) = -\nabla \cdot (\mathbf{u}\phi^{(n)})$ at time level n .

166 4. Results

167 A series of two-dimensional tests are performed over idealised orography. For each test, results
 168 on the BTF, SLEVE and cut cell grid are compared. The first test from Schär et al. (2002) advects
 169 a tracer in a horizontal velocity field. Second, a new tracer advection test is formulated employing
 170 a terrain following velocity field to challenge the advection scheme on cut cell grids. The third

171 test solves the Euler equations for a stably stratified atmosphere initially at rest, following Klemp
 172 (2011). Finally, as specified by Schär et al. (2002), a test of orographically-induced gravity waves
 173 is performed. No explicit diffusion is used in any of the tests.

174 The OpenFOAM implementation of the numerical model, grid generation utilities and test
 175 cases are available at [https://github.com/hertzsprung/tf-cutcell-comparison/tree/](https://github.com/hertzsprung/tf-cutcell-comparison/tree/shaw-weller-2015-mwr)
 176 shaw-weller-2015-mwr.

177 *a. Horizontal advection*

178 Following Schär et al. (2002), a tracer is transported above wave-shaped terrain by solving the
 179 advection equation for a prescribed horizontal wind. This test challenges the accuracy of the
 180 advection scheme in the presence of grid distortions.

181 The domain is 301 km wide and 25 km high, discretized onto a grid with $\Delta x = 1$ km and $\Delta z^* =$
 182 500 m. The domain specified by Schär et al. (2002) is 300 km between the outermost cell centres
 183 where tracer values are specified. In order to reproduce the result from Schär et al. (2002), the
 184 domain has been extended horizontally by $\Delta x/2$ m in both directions so that the distance between
 185 the outermost cell centres is still 300 km.

186 The terrain is wave-shaped, specified by the surface height, h , such that

$$h(x) = h^* \cos^2(\alpha x) \quad (9a)$$

187 where

$$h^*(x) = \begin{cases} h_0 \cos^2(\beta x) & \text{if } |x| < a \\ 0 & \text{otherwise} \end{cases} \quad (9b)$$

188 where $a = 25$ km is the mountain envelope half-width, $h_0 = 3$ km is the maximum mountain height,
 189 $\lambda = 8$ km is the wavelength, $\alpha = \pi/\lambda$ and $\beta = \pi/2a$. On the SLEVE grid, the large-scale com-
 190 ponent h_1 is given by $h_1(x) = h^*(x)/2$ and $s_1 = 15$ km is the large scale height, and $s_2 = 2.5$ km

191 is the small scale height. The optimisation of SLEVE by Leuenberger et al. (2010) is not used, so
 192 the exponent $n = 1$.

193 The wind is entirely horizontal and is prescribed as

$$u(z) = u_0 \begin{cases} 1 & \text{if } z \geq z_2 \\ \sin^2\left(\frac{\pi}{2} \frac{z-z_1}{z_2-z_1}\right) & \text{if } z_1 < z < z_2 \\ 0 & \text{otherwise} \end{cases} \quad (10)$$

194 where $u_0 = 10 \text{ m s}^{-1}$, $z_1 = 4 \text{ km}$ and $z_2 = 5 \text{ km}$. This results in a constant wind aloft, and zero flow
 195 at 4 km and below.

196 To ensure that the discrete velocity field is non-divergent, velocities are prescribed at cell faces
 197 by differencing the streamfunction, Ψ , along the edges from Ψ stored at cell vertices. Since
 198 $u = -\partial\Psi/\partial z$, the streamfunction is found by vertical integration of the velocity profile:

$$\Psi(z) = \frac{u_0}{2} \begin{cases} (2z - z_1 - z_2) & \text{if } z > z_2 \\ z - z_1 - \frac{z_2 - z_1}{\pi} \sin\left(\pi \frac{z - z_1}{z_2 - z_1}\right) & \text{if } z_1 < z \leq z_2 \\ 0 & \text{if } z \leq z_1 \end{cases} \quad (11)$$

199 A tracer, φ , is positioned upstream above the height of the terrain. It has the shape

$$\varphi(x, z) = \varphi_0 \begin{cases} \cos^2\left(\frac{\pi r}{2}\right) & \text{if } r \leq 1 \\ 0 & \text{otherwise} \end{cases} \quad (12)$$

200 having radius, r , given by

$$r = \sqrt{\left(\frac{x - x_0}{A_x}\right)^2 + \left(\frac{z - z_0}{A_z}\right)^2} \quad (13)$$

201 where $A_x = 25 \text{ km}$, $A_z = 3 \text{ km}$ are the horizontal and vertical half-widths respectively, and $\varphi_0 =$
 202 1 is the maximum magnitude of the anomaly. At $t = 0 \text{ s}$, the anomaly is centred at $(x_0, z_0) =$
 203 $(-50 \text{ km}, 9 \text{ km})$ so that the anomaly is upwind of the mountain and well above the maximum
 204 terrain height of 3 km. Analytic solutions can be found by setting the anomaly centre such that
 205 $x_0 = ut$.

206 Unlike Schär et al. (2002) who use periodic lateral boundaries, a fixed value of 0 is used at the
207 inlet boundary and all other boundaries have zero gradient. Furthermore, a second order Runge-
208 Kutta timestepping scheme is used here instead of the leapfrog scheme used by Schär et al. (2002).
209 Tests are integrated forward in time for 10000 s with a timestep of $\Delta t = 25$ s.

210 The test was executed on the BTF, SLEVE and cut cell grids, and on a regular grid with flat
211 terrain using a centred linear scheme and the upwind-biased cubic scheme. Results were also ob-
212 tained on BTF and SLEVE grids with the fourth order scheme from Schär et al. (2002) using a
213 modified version of their Fortran code. The original version of the code interpolated the geometric
214 height at cell vertices from values at adjacent half levels in order to calculate the streamfunction,
215 $\Psi(z)$. The modified version used here directly calculates the height at vertices to enable compar-
216 isons with the finite volume model solutions.

217 Tracer contours at $t = 0$ s, 5000 s and 10000 s are shown in Figure 2. The results are compared
218 on the BTF grid for the centred linear scheme (2a) and the fourth order scheme from Schär et al.
219 (2002) (2c), and the upwind-biased cubic scheme on the cut cell grid (2b), and BTF grid (2d).
220 Tracer errors at $t = 10000$ s are shown for the fourth order and upwind-biased cubic schemes in
221 figures 2e and 2f respectively.

222 By $t = 10000$ s, the tracer suffers from distortion on the BTF grid using the centred linear scheme
223 and some artefacts remain about the mountain peak. The tracer has spread vertically due to in-
224 creased numerical errors when the tracer is transported between layers. Distortions are reduced by
225 using the fourth order scheme from Schär et al. (2002) (figure 2c), but the computational mode is
226 seen as a grid-scale oscillation that travels in the opposite direction to the wind (figure 2e). The re-
227 sults from the centred linear and fourth order schemes are slightly worse than the respective results
228 from Schär et al. (2002) (their figure 6a and figure 8) because of the difference in the discretisation
229 of Ψ .

Using the upwind-biased cubic scheme, tracer magnitude and shape are well-preserved on all grids, both above the mountain at $t = 5000$ s and past the mountain at $t = 10000$ s. In this test, advection is most accurate on the cut cell grid (figure 2b) and regular grid (not shown). As found by Good et al. (2014), the result is the same on both grids. This is to be expected since the wind is zero in the region of the ground and flow aloft is aligned with the grids. On the BTF grid, the tracer is less distorted by the cubic upwind-biased scheme (figure 2d) compared to the centred linear scheme (figure 2a) or fourth order scheme (figure 2c).

Minimum and maximum tracer values and ℓ^2 error norms on the BTF, SLEVE, cut cell and regular grids are summarised in table 1, where the ℓ^2 error norm is defined as

$$\ell^2 = \sqrt{\frac{\sum_c (\varphi - \varphi_T)^2 \mathcal{V}_c}{\sum_c (\varphi_T^2 \mathcal{V}_c)}} \quad (14)$$

where φ is the numerical tracer value, φ_T is the analytic value and \mathcal{V}_c is the cell volume.

The results of the cubic upwind-biased scheme on TF and regular grids are comparable with those for the fourth-order centred scheme from Schär et al. (2002). Error is largest on the BTF grid with $\ell^2 = 0.00791$ but significant reduced on the SLEVE grid with $\ell^2 = 0.00108$. The error is approximately halved by changing from the SLEVE grid to the cut cell grid. Tracer minima and maxima for the centred linear and fourth order schemes are lower than those presented by Schär et al. (2002) because no interpolation is used to calculate the streamfunction.

The centred linear scheme is sensitive to changes in the terrain profile: when the domain width is reduced to 300 km, the ℓ^2 error on the BTF grid rises from 0.0210 to 0.0318. The upwind-biased cubic scheme is less sensitive to the same change, with the ℓ^2 error decreasing from 0.00791 to 0.00767.

250 The results of the horizontal advection test show that numerical errors are due either to mis-
 251 alignment of the flow with the grid, or to grid distortions. Using the upwind-biased cubic scheme,
 252 distortions in the grid do not significantly distort the tracer.

253 *b. Terrain following advection*

254 In the horizontal advection test, results were more accurate where the flow was aligned with
 255 the grid layers, and distortions in the BTF grid led to increased errors. To determine the primary
 256 source of numerical error, we formulate a new tracer advection test in which the velocity field
 257 is everywhere tangential to the basic terrain following coordinate surfaces. Misalignment on the
 258 SLEVE and cut cell grids is designed to challenge the advection scheme.

259 The spatial domain, mountain profile, initial tracer profile and discretisation are the same as
 260 those in the horizontal tracer advection test. The velocity field is defined using a streamfunction,
 261 Ψ , so that the continuous velocity field is non-divergent and follows the BTF coordinate surfaces
 262 given by equation 1 such that

$$\Psi(x, z) = u_0 H \frac{z - h}{H - h} \quad (15)$$

263 where $u_0 = 10 \text{ ms}^{-1}$, which is the horizontal wind speed where $h(x) = 0$. The horizontal and
 264 vertical components of velocity, u and w , are then given by

$$u = \frac{\partial \Psi}{\partial z} = u_0 \frac{H}{H - h}, \quad w = -\frac{\partial \Psi}{\partial x} = u_0 H \frac{dh}{dx} \frac{z - H}{(H - h)^2},$$

$$\frac{dh}{dx} = -h_0 [\beta \cos^2(\alpha x) \sin(2\beta x) + \alpha \cos^2(\beta x) \sin(2\alpha x)] \quad (16)$$

265 Unlike the horizontal advection test, flow extends from the top of the domain all the way to the
 266 ground. The discrete velocity field is calculated using the streamfunction in the same way as the
 267 horizontal advection test.

At $t = 10000$ s the tracer has passed over the mountain. The horizontal position of the tracer centre can be calculated by integrating along the trajectory to find t , the time taken to pass from one side of the mountain to the other:

$$dt = dx/u(x) \quad (17)$$

$$t = \int_0^x \frac{H - h(x)}{u_0 H} dx \quad (18)$$

$$t = \frac{x}{u_0} - \frac{h_0}{16u_0 H} \left[4x + \frac{\sin 2(\alpha + \beta)x}{\alpha + \beta} + \frac{\sin 2(\alpha - \beta)x}{\alpha - \beta} + 2 \left(\frac{\sin 2\alpha x}{\alpha} + \frac{\sin 2\beta x}{\beta} \right) \right] \quad (19)$$

Hence, we find that $x(t = 10000\text{s}) = 51577.4\text{m}$. Because the velocity field is non-divergent, the flow accelerates over mountain ridges and the tracer travels 1577.4m further compared to advection in the purely horizontal velocity field. Tracer height is unchanged downwind of the mountains because advection is along the terrain following coordinate surface.

ℓ^2 errors and tracer extrema for this test are compared with the horizontal advection results in table 1. In the terrain following velocity field, tracer accuracy is greatest on the BTF grid. Using the cubic upwind-biased scheme, errors are about ten times larger on the SLEVE and cut cell grids compared to the BTF grid.

Using the centred linear scheme on the cut cell grid, numerical instability is generated by flow through small cells: when interpolating ϕ onto faces, flux from a large cell into a small cell means that the downwind cell is given greater weighting. The maximum courant number is less than one in all of the advection tests, hence it is not the source of this instability.

We conclude from this test that accuracy depends upon alignment of the flow with the grid, and accuracy is not significantly reduced by grid distortions. Error on the BTF grid in the terrain following advection test is comparable with the error on the SLEVE grid in the horizontal advection test.

287 *c. Stratified atmosphere initially at rest*

288 An idealised terrain profile is defined along with a stably stratified atmosphere at rest in hy-
 289 drostatic balance. The analytic solution is time-invariant, but numerical errors in calculating the
 290 horizontal pressure gradient can give rise to spurious velocities which become more severe over
 291 steeper terrain (Klemp 2011).

292 The test setup follows the specification by Klemp (2011). The grid resolution is $\Delta x = \Delta z^* =$
 293 500 m. All boundary conditions are no normal flow.

294 The wave-shaped mountain profile has a surface height, h , given by

$$h(x) = h_0 \exp\left(-\left(\frac{x}{a}\right)^2\right) \cos^2(\alpha x) \quad (20)$$

295 where $a = 5$ km is the mountain half-width, $h_0 = 1$ km is the maximum mountain height and
 296 $\lambda = 4$ km is the wavelength. For the optimised SLEVE grid, the large-scale component h_1 is
 297 specified as

$$h_1(x) = \frac{1}{2} h_0 \exp\left(-\left(\frac{x}{a}\right)^2\right) \quad (21)$$

298 and, following Leuenberger et al. (2010), $s_1 = 4$ km is the large scale height, $s_2 = 1$ km is the small
 299 scale height, and the optimal exponent value of $n = 1.35$ is used.

300 The initial thermodynamic conditions are in discrete hydrostatic balance, having a reference
 301 potential temperature of $\theta(z = 0) = 288$ K and constant stability with Brunt-Väisälä frequency
 302 $N = 0.01 \text{ s}^{-1}$ everywhere, except for a more stable layer of $N = 0.02 \text{ s}^{-1}$ between $2 \text{ km} \leq z \leq 3 \text{ km}$.
 303 Unlike Klemp (2011), there is no eddy diffusion in the equation set.

304 The test was integrated forward by 5 hours on the BTF, SLEVE and cut cell grids, and a regular
 305 grid with flat terrain. Maximum vertical velocities are presented in figure 3. In agreement with
 306 Klemp (2011), vertical velocities are larger on more distorted grids. However, magnitudes are
 307 smaller comparing results on the terrain following grids with those from Klemp (2011). The results

presented in figure 3, which use a curl-free pressure gradient, have maximum spurious values of w of 0.33 ms^{-1} on the BTF grid, compared with a maximum of $\sim 7 \text{ ms}^{-1}$ found by Klemp (2011) using their improved horizontal pressure gradient formulation. The results in figure 3 have the same maximum errors as Weller and Shahrokhi (2014) but, due to the more stable split into implicitly and explicitly treated terms, the errors decay over time due to the dissipative nature of the advection scheme.

Unlike the result from Klemp (2011), the SLEVE grid does not significantly reduce vertical velocities compared to the BTF grid. However, errors are two orders of magnitude smaller on the cut cell grid with vertical velocities of $\sim 1 \times 10^{-4} \text{ ms}^{-1}$. The smallest error of $\sim 1 \times 10^{-10} \text{ ms}^{-1}$ is found on the regular grid.

Good et al. (2014) found the maximum vertical velocity in their cut cell model was $1 \times 10^{-12} \text{ ms}^{-1}$, which is better than any result obtained using the model by Weller and Shahrokhi (2014). It is worth noting that, in the model used by Good et al. (2014), cell centres are in the centre of the uncut cell, resulting in the centre of some cut cells being below the ground (S.-J. Lock 2014, personal communication). This means that the grid is effectively regular when calculating horizontal and vertical gradients. This would account for the very small velocities found by Good et al. (2014).

In summary, spurious velocities in the resting atmosphere test were similar on both terrain following grids, with lower errors compared to those from Klemp (2011). The maximum vertical velocity was significantly decreased on the cut cell grid, so we conclude that non-orthogonality, or lack of alignment of the grid with surfaces of constant gravitational potential are a significant cause of numerical error in this test.

330 *d. Gravity waves*

331 The test originally specified by Schär et al. (2002) prescribes flow over terrain with small-scale
332 and large-scale undulations which induces propagating and evanescent gravity waves.

333 Following Melvin et al. (2010), the domain is 300 km wide and 30 km high. The mountain
334 profile has the same form as equation 20. Tests are performed with mountain heights of $h_0 = 250$ m
335 and $h_0 = 500$ m. As in the resting atmosphere test, $a = 5$ km is the mountain half-width and
336 $\lambda = 4$ km is the wavelength. On the optimised SLEVE grid, $s_1 = 5$ km is the large scale height,
337 $s_2 = 2$ km is the small scale height and the optimal exponent value $n = 1.35$ is used.

338 The initial thermodynamic conditions have a surface temperature of $\theta(z = 0) = 288$ K and con-
339 stant stability with $N = 0.01 \text{ s}^{-1}$ everywhere. A uniform horizontal wind $u = 10 \text{ m s}^{-1}$ is prescribed
340 at the inlet boundary.

341 Sponge layers are added to the upper 10 km and leftmost 10 km at the inlet boundary to damp
342 the reflection of waves. The term $\mu \rho u$ is subtracted from the momentum (equation 4a) where the
343 damping function, μ , is adapted from Melvin et al. (2010) such that

$$\mu(x, z) = \mu_{\text{upper}} + \mu_{\text{inlet}} \quad (22)$$

$$\mu_{\text{upper}}(z) = \begin{cases} \bar{\mu} \sin^2 \left(\frac{\pi}{2} \frac{z - z_B}{H - z_B} \right) & \text{if } z \geq z_B \\ 0 & \text{otherwise} \end{cases} \quad (23)$$

$$\mu_{\text{inlet}}(x) = \begin{cases} \bar{\mu} \sin^2 \left(\frac{\pi}{2} \frac{x_I - x}{x_I - x_0} \right) & \text{if } x < x_I \\ 0 & \text{otherwise} \end{cases} \quad (24)$$

344 where $\bar{\mu} = 1.2$ is the damping coefficient, $z_B = 20$ km is the bottom of the sponge layer, $H = 30$ km
345 is the top of the domain, $x_0 = -150$ km is the leftmost limit of the domain and $x_I = -140$ km is the

346 rightmost extent of the inlet sponge layer. The sponge layer is only active on faces whose normal
347 is vertical so that it damps vertical momentum only.

348 Note that, while the domain itself is 30 km in height, for the purposes of generating BTF and
349 SLEVE grids, the domain height is set to 20 km because the sponge layer occupies the uppermost
350 10 km.

351 No normal flow is imposed at the top and bottom boundaries and the outlet has a zero gradient
352 boundary condition. For the Exner function of pressure, hydrostatic balance is prescribed on all
353 boundaries. The simulation is integrated forward by 5 hours with a timestep $\Delta t = 8$ s.

354 Test results are compared between the BTF, SLEVE and cut cell grids. Vertical velocities on
355 the BTF, SLEVE and cut cell grids are visually indistinguishable (not shown). They agree with
356 the high resolution mass-conserving semi-implicit semi-Lagrangian solution from Melvin et al.
357 (2010).

358 The initial thermal profile is subtracted from the potential temperature field at the end of the
359 integration to reveal the structure of thermal anomalies. Once again, the results are similar on
360 all three grids, and results are shown on the BTF and cut cell grids in figures 4a and 4c respec-
361 tively. However, examining more closely the anomalies in the lee of the mountain for the cut cell
362 grid, figure 4d shows that the bottommost layer is anomalously warm and the layer above it is
363 anomalously cold. This feature is not present on the BTF grid (figure 4b) or the SLEVE grid (not
364 shown).

365 In a further test, the mountain height is doubled from 250 m to 500 m with all other parameter
366 values unchanged. The same spurious anomaly in potential temperature is again present on the
367 cut cell grid but its amplitude increases. Figure 5 shows vertical profiles of the Exner function of
368 pressure and potential temperature in the lowest 1 km in the lee of the mountain at $x = 50$ km. We
369 find that the decrease in the Exner function of pressure with height is close to linear on all grids.

370 The potential temperature increases linearly with height on the BTF and SLEVE grids. On the cut
371 cell grid, the potential temperature anomalies seen in figure 4d appear as a zig-zag in figure 5.

372 The inaccuracies in potential temperature become invisible when calculating momentum be-
373 cause θ is interpolated onto cell faces, so discrete hydrostatic balance is maintained. This is
374 a manifestation of the Lorenz computational mode (Arakawa and Konor 1996; Holdaway et al.
375 2013). In models that include moist processes, the Lorenz computational mode can disrupt clouds
376 and generate spurious precipitation (Hollingsworth 1995).

377 To summarize, results of the gravity waves test on all grids are in good agreement with the
378 reference solution from Melvin et al. (2010). The most prominent errors are found only on the cut
379 cell grid, where the potential temperature errors near the ground excite the Lorenz computational
380 mode.

381 5. Conclusions

382 We have presented a like-for-like comparison between terrain following and cut cell grids using
383 a single model. Accuracy on the BTF, SLEVE and cut cell grids was evaluated in a series of
384 two-dimensional tests.

385 Across all tests, a high degree of accuracy was achieved for all grids. Even on the highly-
386 distorted BTF grid, which have previously been found to give poor results (Schär et al. 2002;
387 Klemp 2011; Good et al. 2014), errors were often small in the tests presented here. In the first two
388 tests, tracers were advected by horizontal and terrain following velocity fields. We found that the
389 accuracy of the upwind-biased cubic advection scheme depended upon alignment of the flow with
390 the grid rather than on grid distortions.

391 Spurious vertical velocities were small in the resting initial state test, reaching a maximum of
392 $\sim 0.35 \text{ ms}^{-1}$ on the BTF grid, compared to a maximum of $\sim 7 \text{ ms}^{-1}$ found by Klemp (2011). In

the gravity waves test, vertical velocities were in good agreement with the reference solution from Melvin et al. (2010) across all grids.

Cut cell grids reduced errors in two of the four tests. First, in the horizontal advection test, tracer accuracy on the cut cell grid was almost as good as accuracy on a regular grid with no mountain. Second, in the resting atmosphere test, spurious vertical velocities were two orders of magnitude smaller on the cut cell grid compared with the terrain following grids.

Conversely, in the terrain following advection test, errors were large on the SLEVE and cut cell grids where velocities were misaligned with the grids. In the gravity waves test, the Lorenz computational mode was manifested as a zig-zag in potential temperature in the lowest layers in the lee of the mountain. This spurious error was excited only on the cut cell grid. This test motivates further work to formulate a Charney–Phillips staggering of variables on cut cell grids.

Acknowledgments. I am grateful to my co-supervisors John Methven and Terry Davies for their valuable input, and to Christoph Schär (ETH) for his assistance in reproducing his advection test results. I am thankful for the NERC studentship which helped fund this work. Weller is funded by NERC grant NE/H015698/1.

References

Adcroft, A., C. Hill, and J. Marshall, 1997: Representation of topography by shaved cells in a height coordinate ocean model. *Mon. Wea. Rev.*, **125**, 2293–2315.

Arakawa, A., and C. S. Konor, 1996: Vertical differencing of the primitive equations based on the charney-phillips grid in hybrid σ – p vertical coordinates. *Mon. Wea. Rev.*, **124**, 511–528.

Fast, J. D., 2003: Forecasts of valley circulations using the terrain-following and step-mountain vertical coordinates in the meso-eta model. *Wea. Forecasting*, **18**, 1192–1206.

415 Gal-Chen, T., and R. C. Somerville, 1975: On the use of a coordinate transformation for the
 416 solution of the navier-stokes equations. *J. Comp. Phys.*, **17**, 209–228.

417 Gallus, W. A., and J. B. Klemp, 2000: Behavior of flow over step orography. *Mon. Wea. Rev.*, **128**,
 418 1153–1164.

419 Gary, J. M., 1973: Estimate of truncation error in transformed coordinate, primitive equation
 420 atmospheric models. *J. Atmos. Sci.*, **30**, 223–233.

421 Good, B., A. Gadian, S.-J. Lock, and A. Ross, 2014: Performance of the cut-cell method of
 422 representing orography in idealized simulations. *Atmos. Sci. Lett.*, **15**, 44–49.

423 Holdaway, D., J. Thuburn, and N. Wood, 2013: Comparison of Lorenz and Charney–Phillips
 424 vertical discretisations for dynamics–boundary layer coupling. Part II: Transients. *Quart. J. Roy.*
 425 *Meteor. Soc.*, **139**, 1087–1098.

426 Hollingsworth, A., 1995: *A Spurious Mode in the ‘Lorenz’ Arrangement of f and T which Does*
 427 *Not Exist in the ‘Charney–Phillips’ Arrangement*. European Centre for Medium-Range Weather
 428 Forecasts.

429 Jebens, S., O. Knoth, and R. Weiner, 2011: Partially implicit peer methods for the compressible
 430 euler equations. *J. Comp. Phys.*, **230**, 4955–4974.

431 Klein, R., K. Bates, and N. Nikiforakis, 2009: Well-balanced compressible cut-cell simulation of
 432 atmospheric flow. *Philos. Trans. Roy. Soc. London*, **367**, 4559–4575.

433 Klemp, J. B., 2011: A terrain-following coordinate with smoothed coordinate surfaces. *Mon. Wea.*
 434 *Rev.*, **139**, 2163–2169.

435 Leuenberger, D., M. Koller, O. Fuhrer, and C. Schär, 2010: A generalization of the SLEVE vertical
 436 coordinate. *Mon. Wea. Rev.*, **138**, 3683–3689.

437 Melvin, T., M. Dubal, N. Wood, A. Staniforth, and M. Zerroukat, 2010: An inherently mass-
 438 conserving iterative semi-implicit semi-lagrangian discretization of the non-hydrostatic vertical-
 439 slice equations. *Quart. J. Roy. Meteor. Soc.*, **136**, 799–814.

440 Mesinger, F., Z. I. Janjić, S. Ničkovic, D. Gavrilov, and D. G. Deaven, 1988: The step-mountain
 441 coordinate: Model description and performance for cases of alpine lee cyclogenesis and for a
 442 case of an appalachian redevelopment. *Mon. Wea. Rev.*, **116**, 1493–1518.

443 Mesinger, F., and Coauthors, 2012: An upgraded version of the eta model. *Meteor. Atmos. Phys.*,
 444 **116**, 63–79.

445 OpenCFD Foundation, cited 2015: OpenFOAM® – User Guide. [Available online at [http://cfd.](http://cfd.direct/openfoam/user-guide/snappyhexmesh/#x26-1510005.4)
 446 [direct/openfoam/user-guide/snappyhexmesh/#x26-1510005.4](http://cfd.direct/openfoam/user-guide/snappyhexmesh/#x26-1510005.4)].

447 Phillips, N. A., 1957: A coordinate system having some special advantages for numerical fore-
 448 casting. *J. Meteor.*, **14**, 184–185.

449 Schär, C., D. Leuenberger, O. Fuhrer, D. Lüthi, and C. Girard, 2002: A new terrain-following
 450 vertical coordinate formulation for atmospheric prediction models. *Mon. Wea. Rev.*, **130**, 2459–
 451 2480.

452 Simmons, A. J., and D. M. Burridge, 1981: An energy and angular-momentum conserving vertical
 453 finite-difference scheme and hybrid vertical coordinates. *Mon. Wea. Rev.*, **109**, 758–766.

454 Steppeler, J., H.-W. Bitzer, M. Minotte, and L. Bonaventura, 2002: Nonhydrostatic atmospheric
 455 modeling using a z -coordinate representation. *Mon. Wea. Rev.*, **130**, 2143–2149.

456 Steppeler, J., R. Hess, U. Schättler, and L. Bonaventura, 2003: Review of numerical methods for
 457 nonhydrostatic weather prediction models. *Meteor. Atmos. Phys.*, **82**, 287–301.

458 Steppeler, J., S.-H. Park, and A. Dobler, 2013: Forecasts covering one month using a cut-cell
 459 model. *Geosci. Model Dev.*, **6**, 875–882.

460 Webster, S., A. Brown, D. Cameron, and C. Jones, 2003: Improvements to the representation of
 461 orography in the met office unified model. *Quart. J. Roy. Meteor. Soc.*, **129**, 1989–2010.

462 Weller, H., and A. Shahrokhi, 2014: Curl free pressure gradients over orography in a solution of
 463 the fully compressible euler equations with implicit treatment of acoustic and gravity waves.
 464 *Mon. Wea. Rev.*, **142**, 4439–4457.

465 Yamazaki, H., and T. Satomura, 2010: Nonhydrostatic atmospheric modeling using a combined
 466 cartesian grid. *Mon. Wea. Rev.*, **138**, 3932–3945.

467 Zängl, G., 2012: Extending the numerical stability limit of terrain-following coordinate models
 468 over steep slopes. *Mon. Wea. Rev.*, **140**, 3722–3733.

469 **LIST OF TABLES**

470 **Table 1.** Minimum and maximum tracer magnitudes and ℓ^2 error norms (defined by
471 equation 14) at $t = 10\,000$ s in the horizontal and terrain following tracer advec-
472 tion tests using centred linear and cubic upwind-biased schemes. For the hor-
473 izontal advection test, minimum and maximum values are given for the fourth
474 order scheme using the modified code from Schär et al. (2002). ℓ^2 error norms
475 were not calculated by this code. 26

TABLE 1. Minimum and maximum tracer magnitudes and ℓ^2 error norms (defined by equation 14) at $t = 10000$ s in the horizontal and terrain following tracer advection tests using centred linear and cubic upwind-biased schemes. For the horizontal advection test, minimum and maximum values are given for the fourth order scheme using the modified code from Schär et al. (2002). ℓ^2 error norms were not calculated by this code.

			Analytic	BTF	SLEVE	Cut cell	No terrain
Horizontal	Centred linear	ℓ^2 error	0	0.0210	0.00233	0.00224	0.00223
		min	0	-0.275	-0.0252	-0.0251	-0.0251
		max	1	0.925	0.985	0.985	0.985
	Fourth order	min	0	-0.0926	-0.00174	—	-0.00178
		max	1	1.00	0.984	—	0.983
	Cubic upwind-biased	ℓ^2 error	0	0.00791	0.00108	0.000577	0.000576
		min	0	-0.0446	-0.0106	-0.000674	-0.00674
		max	1	0.925	0.982	0.983	0.983
Terrain following	Centred linear	ℓ^2 error	0	0.00251	0.0173	13.6	—
		min	0	-0.0245	-0.120	-623	—
		max	1	0.985	0.950	3480	—
	Cubic upwind-biased	ℓ^2 error	0	0.00154	0.0120	0.0134	—
		min	0	-0.0110	-0.0263	-0.028	—
		max	1	0.983	0.865	0.851	—

LIST OF FIGURES

- Fig. 1.** Examples of (a) BTF, (b) SLEVE, and (c) a cut cell grid, showing cell edges in the lowest four layers. The full two dimensional grids are 20 km wide and 20 km high. SLEVE parameters are specified in the resting atmosphere test in section 4c. The cut cell grid was created by intersecting the terrain surface with a regular grid as described in section 2. Axes are in units of m. 28
- Fig. 2.** Horizontally advected tracer contours at $t = 0$ s, 5000 s and 10000 s using (a) centred linear scheme on the BTF grid, (b) the upwind-biased cubic scheme on the cut cell grid, (c) the fourth order scheme from Schär et al. (2002) on the BTF grid, and (d) the upwind-biased cubic scheme on the BTF grid with contour intervals every 0.1. Errors on the BTF grid at $t = 10000$ s are shown for (e) the fourth order scheme from Schär et al. (2002), and (f) the upwind-biased cubic scheme, with contour intervals every 0.01. Negative contours denoted by dotted lines. The terrain profile is also shown immediately above the x axis. Subfigures (c) and (e) produced using the modified version of the code from Schär et al. (2002). 29
- Fig. 3.** Maximum spurious vertical velocity, w (m s^{-1}), in the resting atmosphere test with results on BTF, SLEVE, cut cell and regular grids using the model from Weller and Shahrokhi (2014) which includes a curl-free pressure gradient formulation. 30
- Fig. 4.** Anomalies in potential temperature in the gravity waves test after 5 hours with a mountain height, $h_0 = 250$ m. The central domain in the lowest 12 km is shown on (a) the BTF grid, and (c) the cut cell grid. The four lowest layers of each grid are shown for (b) BTF, and (d) cut cell grids, using a narrower potential temperature scale. The results on the SLEVE grid (not shown) are qualitatively identical to results on the BTF grid. Axes are in units of m. 31
- Fig. 5.** Vertical profiles of the Exner function of pressure, Π , and potential temperature, θ , in the gravity waves test with a mountain height of $h_0 = 500$ m. The Exner profile is visually identical on all grids for both mountain heights; for clarity, the Exner profile is only plotted for the BTF grid. The Lorenz computational mode is manifested as a zig-zag in potential temperature on the cut cell grid. Results on the SLEVE grid (not shown) are qualitatively the same as those on the BTF grid. The thermal profile with a lesser mountain height of $h_0 = 250$ m (not shown) exhibits a computational mode with smaller amplitude. 32

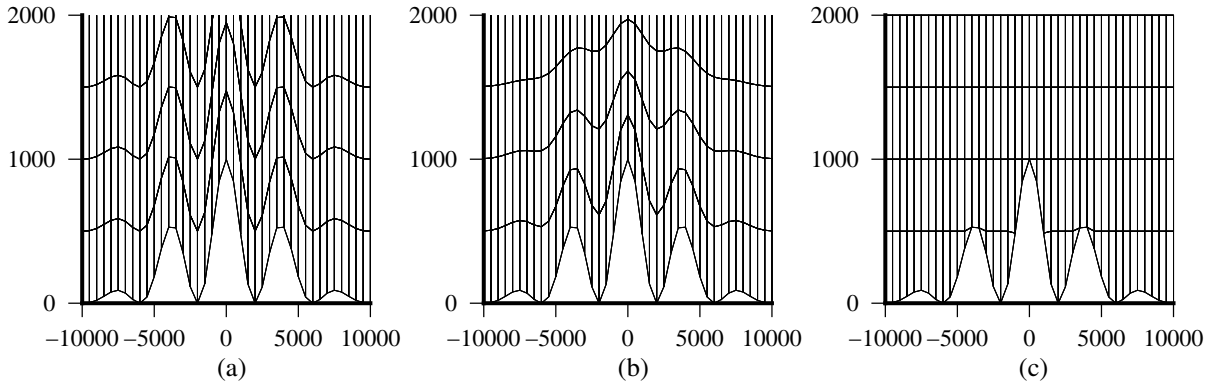


FIG. 1. Examples of (a) BTF, (b) SLEVE, and (c) a cut cell grid, showing cell edges in the lowest four layers. The full two dimensional grids are 20 km wide and 20 km high. SLEVE parameters are specified in the resting atmosphere test in section 4c. The cut cell grid was created by intersecting the terrain surface with a regular grid as described in section 2. Axes are in units of m.

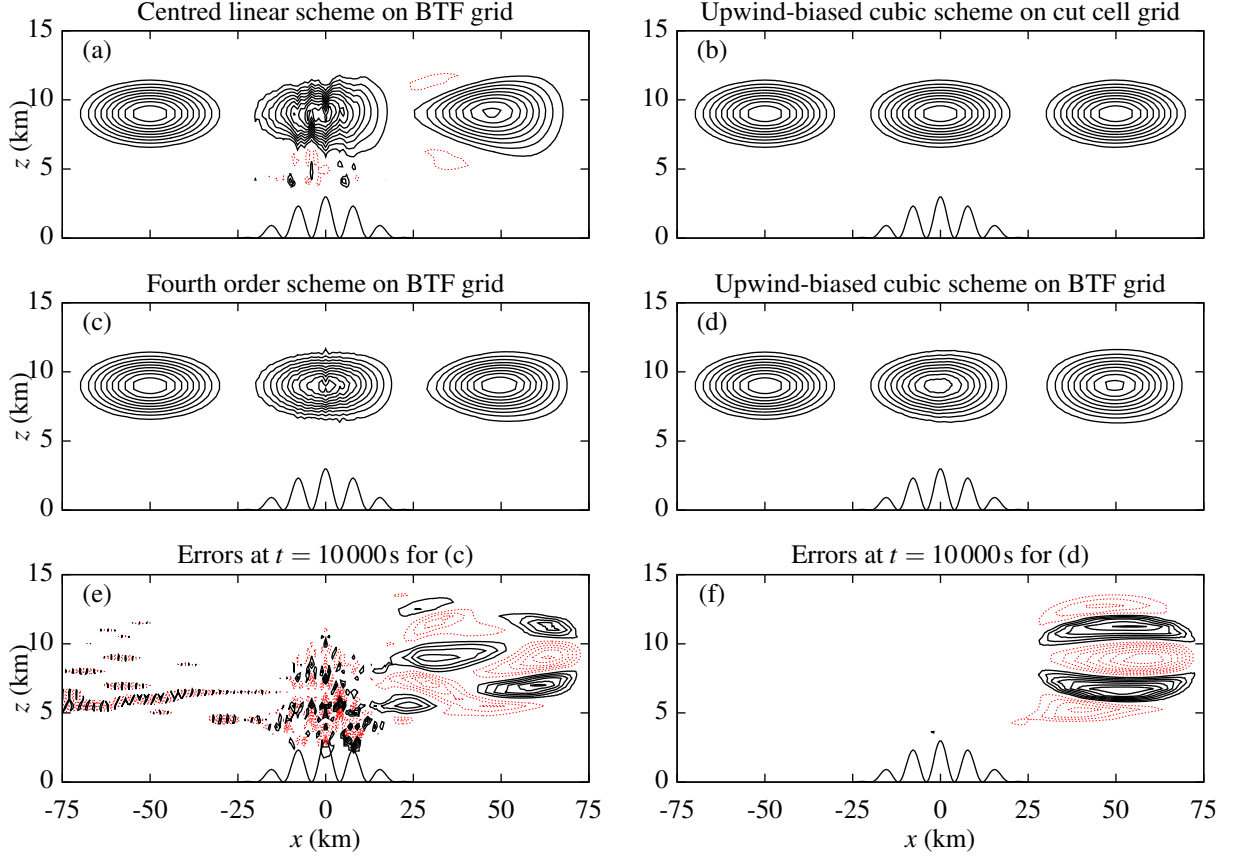


FIG. 2. Horizontally advected tracer contours at $t = 0$ s, 5000 s and 10000 s using (a) centred linear scheme on the BTF grid, (b) the upwind-biased cubic scheme on the cut cell grid, (c) the fourth order scheme from Schär et al. (2002) on the BTF grid, and (d) the upwind-biased cubic scheme on the BTF grid with contour intervals every 0.1. Errors on the BTF grid at $t = 10000$ s are shown for (e) the fourth order scheme from Schär et al. (2002), and (f) the upwind-biased cubic scheme, with contour intervals every 0.01. Negative contours denoted by dotted lines. The terrain profile is also shown immediately above the x axis. Subfigures (c) and (e) produced using the modified version of the code from Schär et al. (2002).

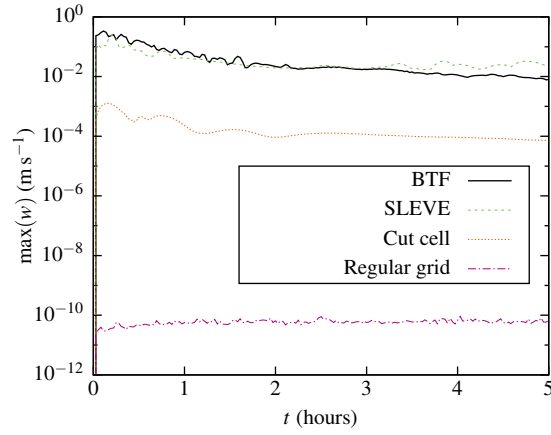


FIG. 3. Maximum spurious vertical velocity, w (m s^{-1}), in the resting atmosphere test with results on BTF, SLEVE, cut cell and regular grids using the model from Weller and Shahrokhi (2014) which includes a curl-free pressure gradient formulation.

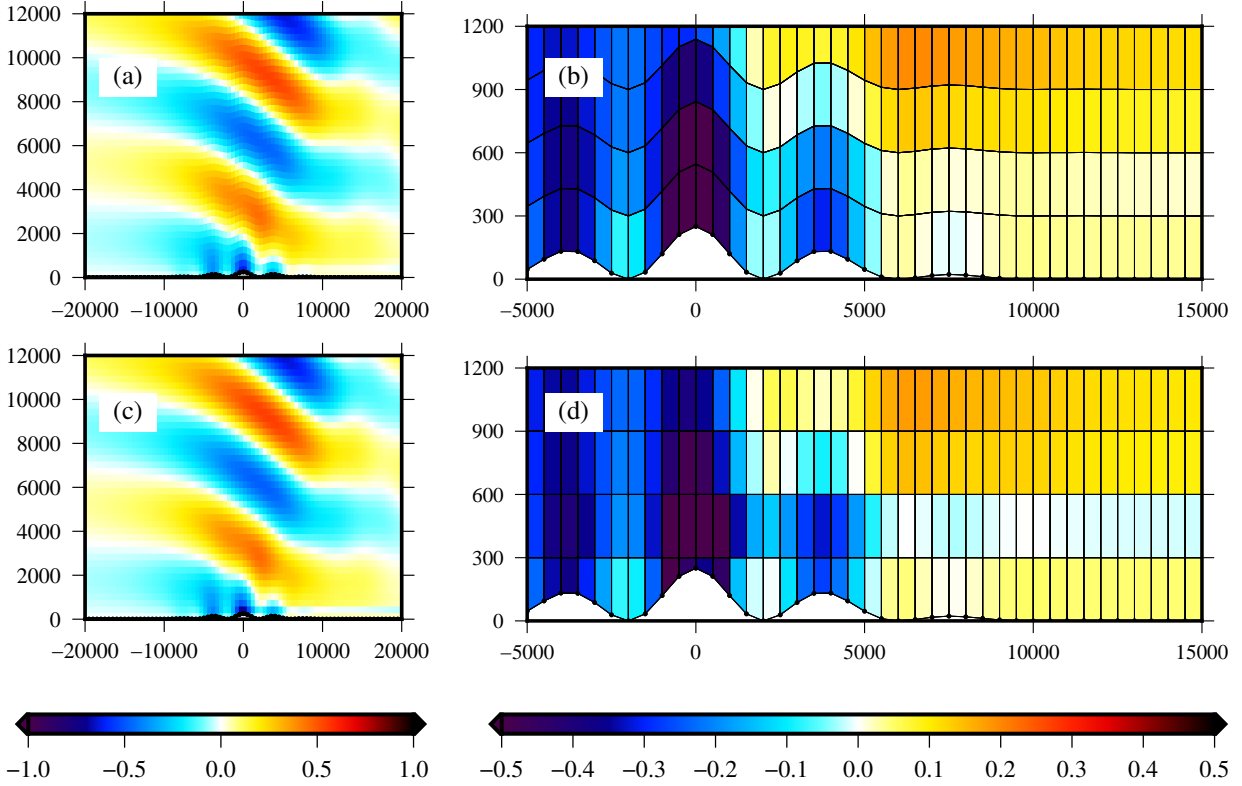
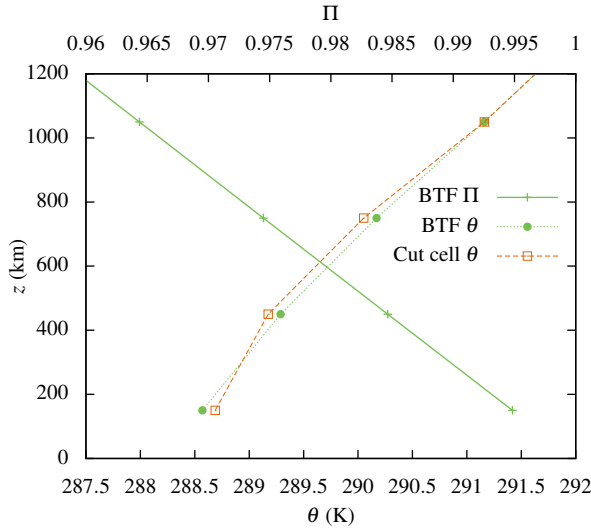


FIG. 4. Anomalies in potential temperature in the gravity waves test after 5 hours with a mountain height, $h_0 = 250\text{m}$. The central domain in the lowest 12 km is shown on (a) the BTF grid, and (c) the cut cell grid. The four lowest layers of each grid are shown for (b) BTF, and (d) cut cell grids, using a narrower potential temperature scale. The results on the SLEVE grid (not shown) are qualitatively identical to results on the BTF grid. Axes are in units of m.



528 FIG. 5. Vertical profiles of the Exner function of pressure, Π , and potential temperature, θ , in the gravity
 529 waves test with a mountain height of $h_0 = 500\text{m}$. The Exner profile is visually identical on all grids for both
 530 mountain heights; for clarity, the Exner profile is only plotted for the BTF grid. The Lorenz computational
 531 mode is manifested as a zig-zag in potential temperature on the cut cell grid. Results on the SLEVE grid (not
 532 shown) are qualitatively the same as those on the BTF grid. The thermal profile with a lesser mountain height of
 533 $h_0 = 250\text{m}$ (not shown) exhibits a computational mode with smaller amplitude.